Contents lists available at SciVerse ScienceDirect

Corrosion Science

journal homepage: www.elsevier.com/locate/corsci

Atmospheric corrosion of Galfan coatings on steel in chloride-rich environments

Xian Zhang, Christofer Leygraf, Inger Odnevall Wallinder *

KTH Royal Institute of Technology, Div. Surface and Corrosion Science, School of Chemical Science and Engineering, Dr. Kristinas v. 51, SE-100 44 Stockholm, Sweden

ABSTRACT

Galfan coatings on steel in laboratory exposures with predeposited NaCl and cyclic wet/dry conditions exhibit nearly the same corrosion products as after 5 years of marine exposure. A general scenario for corrosion product evolution on Galfan in chloride-rich atmospheres is proposed. It includes the initial formation of ZnO, $ZnAl_2O_4$ and Al_2O_3 and subsequent formation of $Zn_6Al_2(OH)_{16}CO_3 \cdot 4H_2O$, and $Zn_2Al(OH)_6Cl \cdot 2H_2O$ and/or $Zn_5Cl_2(OH)_8 \cdot H_2O$. An important phase is $Zn_6Al_2(OH)_{16}CO_3 \cdot 4H_2O$, which largely governs the reduced long-term zinc runoff from Galfan. A clear influence of microstructure could be observed on corrosion initiation in the slightly zinc-richer η-Zn phase adjacent to the β-Al phase.

© 2013 Elsevier Ltd. All rights reserved.

1. Introduction

Hot-dip galvanized coatings containing aluminum on steel substrates have been frequently used in automotive, construction and other industrial applications [1]. One example is the commercial Zn–Al alloy coating on steel (Zn–5 wt.% Al, trade name Galfan™, from now on called Galfan), which is commonly used in automotive applications due to its high corrosion resistance properties, superior ductility and forming properties [2]. This coating contains 5 wt.% Al, which is very close to the eutectic point (6 wt.% Al) in the Zn–Al system [3,4], and up to 0.05 wt.% mischmetal (lanthamum and cerium). The microstructure of the Galfan coating is generally characterized by a two-phase structure, a zinc-rich proeutectoid phase (<5 wt.% Al/(Al + Zn)) surrounded by an eutectic phase (5–10 wt.% Al/(Al + Zn)) consisting of beta (β) aluminum (5–25 wt.% Al) and eta (η) zinc lamellas (<5 wt.% Al) [5–8]. Since the microstructure depends on several factors such as cooling rate, annealing time and nucleation temperature in the solidification process, these factors may also influence the corrosion resistance of Galfan [9–11].

Atmospheric corrosion of zinc in natural weathering conditions has been widely investigated [12–16]. A general evolution scheme of corrosion product formation on zinc was established by Odnevall and Leygraf [17]. A thin layer of amorphous hydroxycarbonate (Hydrozincite, $Zn_5(OH)_6CO_3$) forms rapidly in any humid-containing atmosphere. In humid, low polluted environments, this phase often gradually evolves into its crystalline form. If chlorides are also present in the atmosphere, zinc hydroxychloride (Simonkolleite, $Zn_5(OH)_8Cl_2 \cdot H_2O$) is locally formed and eventually evolves into a sodium zinc hydroxychlorosulfate (Gordaite, $Na_4Zn_4SO_4(OH)_6Cl_2 \cdot 6H_2O$). A large number of studies have investigated the atmospheric corrosion of zinc by means of laboratory-simulated exposures [18–20]. Chen et al. studied the effect of NaCl-induced atmospheric corrosion of zinc metal by using an experimental set-up for in situ analysis, with $Zn_5(OH)_8Cl_2 \cdot H_2O$ as the main corrosion product identified [21].

Significant knowledge exists concerning the atmospheric corrosion of zinc–aluminum coatings on steel in terms of corrosion rates and long-term corrosion product formation [16,22–25], especially for the Zn–55 wt.% Al coating Galvalume™ (from now on denoted Galvalume) on steel and for Galfan. Besides zinc-based corrosion products, $Zn_6Al_2(OH)_{16}CO_3 \cdot 4H_2O$ has been identified in several investigations [26–28] as well as $Zn_2Al(OH)_6Cl \cdot 2H_2O$ [29]. In previous studies by some of the authors, Galvalume was investigated with respect to metal release and corrosion product evolution during short and long term atmospheric exposures [30,31]. Due to its relative simple microstructure, compared to Galfan, corrosion initiation of Galvalume was taking place in the zinc-rich interdentritic phases, whereas the aluminum-rich dentritic phases only corroded after longer exposure periods or in more severe environments [32]. Galfan has a much more complex and fine (sub-micron sized) microstructure compared with Galvalume, which may explain why very little is reported regarding its initial corrosion behavior during early stages of atmospheric corrosion and any possible correlation to its heterogeneous microstructure. Tang et al. [33] found

---

* Corresponding author. Tel.: +46 8 790 6621; fax: +46 8 208284.
 E-mail address: ingero@kth.se (I. Odnevall Wallinder).

that the proeutectoid η-Zn phase possesses improved corrosion resistance compared with the eutectic colonies. Yang and co-workers [34] proposed a corrosion model in which the eutectic phase was prone to preferential attack when superplastic Zn–Al alloys (4, 8, 12, 16 wt.% Al) were immersed in simulated acid rain.

This study aims to investigate the initial atmospheric corrosion mechanism and corrosion product evolution of Galfan and how this may be influenced by the microstructure. The work forms part of a larger research investigation in which one of the targets is to evaluate an accelerated corrosion test of Zn–Al coatings on steel for automotive applications, the N-VDA-test [35], from a corrosion product formation perspective. Through successive short-term controlled laboratory exposures the influence of humidity and chlorides has been elucidated by using a combination of near surface- and bulk sensitive analytical tools. Generated results have been compared with long-term data from a 5-year marine field exposure. By considering obtained corrosion product data, a general model for the evolution of corrosion products of Zn–Al coatings exposed to low-polluted humid conditions and chloride-rich environments has been proposed.

2. Materials and methods

2.1. Material and surface preparation

Non-treated Galfan (95 wt.% Zn–5 wt.% Al with additions of 0.05 wt.% cerium and lanthanum) samples were supplied from Arcelor Mittal, France. The 7 μm coating on steel was applied via a hot-dip process [2]. No mischmetal was observed in the corrosion products. The samples were cut to a dimension of 10×10 mm and most samples were gently polished using a 0.25 μm diamond paste to remove the utmost high temperature oxide layer formed during the hot-dip process. Prior to the experiments, each sample was ultrasonically cleaned in analytical grade ethanol for 10 min and dried by cold nitrogen gas before stored in a desiccator overnight.

2.2. Laboratory wet/dry cycle exposure conditions and in situ surface characterization

Parallel in situ experiments were carried out by means of ESEM (environmental–scanning electron microscopy) and in situ IRAS (Infrared Reflection Absorption Spectroscopy) on Galfan samples exposed to the following cyclic exposure conditions: NaCl pre-deposition (0 or 4 μg NaCl/cm²), the first cycle 4 h (RH 90%) and 2 h (RH 0%), the second cycle 16 h (RH 90%) and 2 h (RH 0%). These cycles were repeated several times. Parallel exposures were conducted at 70% RH.

SEM imaging of surface features and IRAS spectra of corrosion product formation were generated during the dry cycles. Prior to exposure, NaCl (in a saturated 99.5% ethanol solution) was applied onto the surfaces by means of a transfer pipette. Upon ethanol evaporation, NaCl crystals were relatively homogeneously distributed over the surface. The amount of deposited NaCl was weighed by means of a microbalance (Mettler Toledo Excellence) and normalized to the geometric surface area of the samples. Detailed information of the procedure for pre-deposition of NaCl is given elsewhere [36].

Environmental scanning electron microscopy/energy dispersive X-ray analysis (ESEM/EDS) was performed using a FEI – XL 30 Series instrument, equipped with an EDAX Phoenix EDS system with an ultra-thin windows Si–Li detector. The relative humidity (RH) of the chamber was gradually increased to 70% and 90%, respectively. The acquired RH was obtained by controlling the temperature and pressure by means of a thermoelectric stage controller. Images were generated using gaseous secondary electron (GSE) detector.

To increase the resolution, images were in addition generated ex situ, switching to the normal secondary electron (SE)/backscatter electron (BSE) detector. All images (75% SE and 25% BSE) were collected using an accelerating voltage of 15 or 30 kV.

In situ infrared reflection absorption spectroscopy (IRAS) was performed in a humidity chamber on samples with and without pre-deposited NaCl. Controlled humidified conditions were obtained by mixing dry and wet pre-cleaned compressed air of reduced CO_2 (lower than 20 ppm). Experimental details are given elsewhere [37]. The IRAS spectra were recorded using a commercial Digilab 4.0 Pro FTIR spectrometer, acquiring 1024 scans with a resolution of 4 cm^{-1} for each spectrum. The results are presented in absorbance units ($-\log(R/R_0)$), where R is the reflectance of the exposed sample surface and R_0 the reflectance of the non-exposed sample [19].

2.3. Long-term field exposure

The same batch of non-treated Galfan surfaces as investigated in the laboratory exposure were exposed at unsheltered conditions at the marine site of Brest, France for 5 years (SO$_2$ < 3 μg m^{-3}, precipitation 800–1000 mm year^{-1}). Time-resolved measurements were conducted to assess the evolution of corrosion products (2, 4, 12, 26 and 52 weeks, 5 years). The release of zinc from the patina was determined during the 5-year period by continuously collecting and analysing the zinc concentration in the collected runoff water. All surfaces were exposed 5–10 m from the waterline at the marine site of Sainte Anne du Portzic, a cape outside the city of Brest, on the northwest coast of France. The materials were exposed at an inclination of 45° from the horizontal, facing south, according to the ISO 17752 standard for metal runoff rate measurements [38]. More detailed information of the test site is given elsewhere [39,40].

2.4. Ex situ surface characterization

A multitude of surface sensitive and non-destructive analytical methods were adopted for detailed ex situ analysis of corrosion product formation. Scanning electron microscopy and energy dispersive spectroscopy (FEG-SEM/EDS) were employed for morphological and compositional investigations, infrared (IRAS) and confocal Raman micro-spectroscopy (CRM) for information of functional surface groups and possibly their lateral distribution. Surface sensitive grazing incidence X-ray diffraction (GIXRD) was used for the detection of crystalline phases.

FEG-SEM/EDS analysis was conducted by using a LEO 1530 instrument with a Gemini column, upgraded to a Zeiss Supra 55
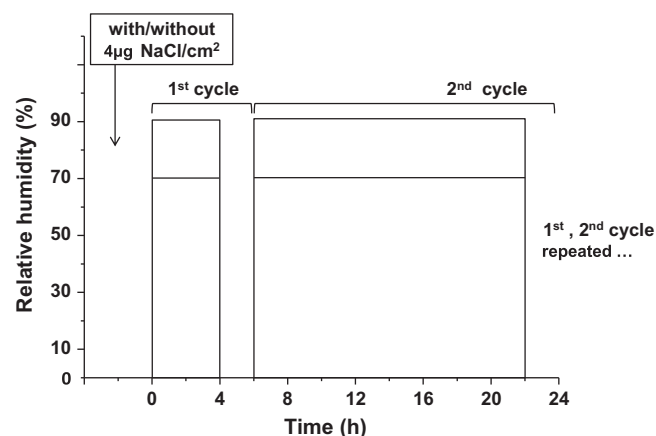

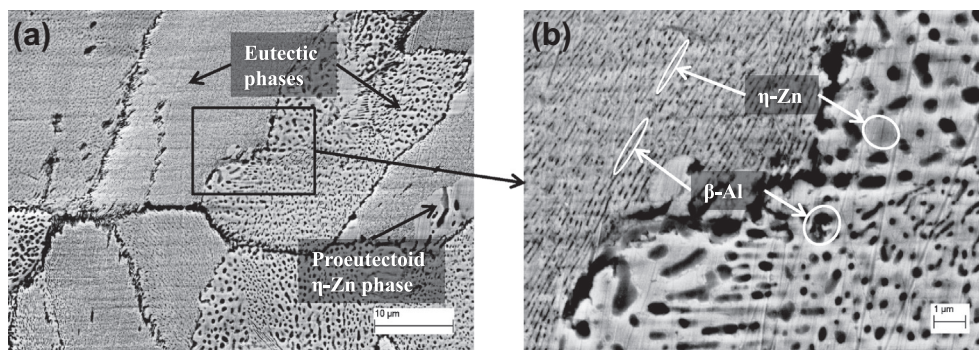**Fig. 1.** Wet/dry cycle exposure conditions during laboratory exposures.

Fig. 2. SEM images showing the microstructure of unexposed diamond-polished Galfan at (a) lower and (b) higher magnification.

(equivalent) and an EDS X-Max SDD (Silicon Drift Detector) 50 mm² detector from Oxford Instruments. The SEM settings were 15 kV using an aperture size of 60 µm.

CRM measurements were carried out using a WITec alpha 300 system, equipped with a laser source of wavelength 532 nm. The integration time per Raman spectrum was in the order of 50 ms. Measurements were obtained with a Nikon objective, Nikon NA0.9 NGC, together with a pinhole of 100 µm diameter. The Raman spectra were produced in the scanning area with lateral and vertical resolutions of approximately 300 nm and 2 µm, respectively.

GIXRD analyses were made by using an X'pert PRO PANALYTI-CAL system, equipped with an X-ray mirror (Cu Kα radiation) and a 0.27° parallel plate collimator on the diffracted side. The surface scanning area was 1×1 cm at a grazing angle of 88° versus the surface.

3. Results

3.1. Effect of humidity on initial corrosion of Galfan

In this first part of the investigation, the microstructure of Galfan is presented. It is followed by two parallel laboratory exposures at cyclic humidity conditions monitoring changes in surface feature morphologies by means of SEM, and compositional changes by in situ IRAS.

Fig. 2 exhibits the microstructure of diamond polished Galfan visualized by means of SEM at low magnification (left). It displays two different regions, the dominating eutectic phase and a zinc-rich proeutectoid phase (η-phase, indicated in the figure) [5,6]. As the eutectic phase is regarded as the most susceptible phase for corrosion initiation [33,34], the main focus of this investigation lies in this area. The microstructure is also visualized in Fig. 2 at higher magnification (right), where the eutectic structure clearly is seen as lamellas or rods (dark grey in the image) surrounded by a matrix (light grey in the image). In accordance with designations reported in the literature [5,41], we from now on denote the lamellas or rods "β-Al" and the surrounding light greyish areas "η-Zn". Spot-analyses by means of EDS show a slightly higher aluminum content (elemental mass ratio Al/(Al + Zn) > 5%) of the β-Al phase compared with the surrounding η-Zn matrix (Al/(Al + Zn) < 5%).

Fig. 3 displays SEM-images of Galfan before (a) and after exposure to one (b and c) and two (d) wet/dry cycles at 90% RH, respectively. When comparing the same area in Fig. 3a and b, it is evident that the first wet/dry cycle exposure (5 h in total, Fig. 1) resulted in the formation of a few thread-like corrosion products predominantly at the η-Zn phase, adjacent to the aluminum-richer β-Al phase. In a few cases, Fig. 3c, the corrosion products formed larger

clusters. When following such a cluster from the periphery towards its center, it can be concluded that the thread-like corrosion products illustrated in Fig. 3b also were present in peripheric areas adjacent to the β-Al phase. According to EDS measurements at the center of the cluster, Al, Zn, O and C were the main elemental constituents.

After the second wet/dry cycle (up to 23 h in Fig. 1), thread-like corrosion products covered the entire surface, independent of microstructural phases, seen as whitish features in Fig. 3d, also with some cluster-like morphologies. Their size and thickness did not allow any further compositional analysis by means of EDS. For this reason, the growth and evolution of these corrosion products were monitored in parallel exposures by means of IRAS, investigations that allow an overall analysis of the exposed surface region under current in situ conditions with an information depth of 100 nm or more [42], however with no lateral resolution during the chemical analysis.

Fig. 4 exhibits the IRAS spectra in the lower wavenumber range from 500 up to 1500 cm⁻¹ obtained after one and two wet/dry cycles at 90% RH, respectively. After the first cycle (lower curve) at least four peaks were identified, all indicated by arrows in the figure. Starting from lower wavenumber and going upwards the peak at 525 cm⁻¹ was attributed to the zinc–oxygen bond in ZnO [21]. The next peak at around 792 cm⁻¹ may originate from the bending mode of either Zn–O–H and/or Al–O–H [26]. The weak and broad band at 945 cm⁻¹ may originate from Al_2O_3 [30], while the broad band in the range from 1250 to 1400 cm⁻¹ most likely originates from anti-symmetric stretching modes of carbonate (CO_3^{2-}) [43]. The exact location of this band reflects the phase from which it originates. When located at around 1350 cm⁻¹ it has been assigned to Hydrotalcite ($Zn_6Al_2(OH)_{16}CO_3 \cdot 4H_2O$), a zinc aluminum hydroxycarbonate, which has been reported to form on Zn–Al coatings in marine environments [26,44]. When located around 1450 cm⁻¹ the carbonate band has been assigned to Hydrozincite ($Zn_5(CO_3)_2(OH)_6$) [43], a phase formed in early stages and in humid conditions of atmospheric corrosion of zinc metal and galvanized steel [17,45]. When combining the IRAS results after one cycle with corresponding SEM-images we tentatively propose the thread-like corrosion products to consist of ZnO and/or $Zn_6Al_2(OH)_{16}CO_3 \cdot 4H_2O$.

After two wet/dry cycles (upper curve) the peaks that were attributed to ZnO, Zn–O–H or Al–O–H (now represented by two more peaks at 900 and 1015 cm⁻¹) and CO_3^{2-} (now with more clearly resolved peaks, including a main peak in the range of 1270–1370 cm⁻¹) increased in amplitude, while the peak from Al_2O_3 was suppressed. Instead new peaks appeared in the range of 560–680 cm⁻¹, tentatively assigned to $ZnAl_2O_4$ [46,47], a possible corrosion product for Zn–Al alloys [48]. The latter exists most likely in its amorphous form since crystalline $ZnAl_2O_4$ only can be synthesized at elevated temperatures [46]. When combining
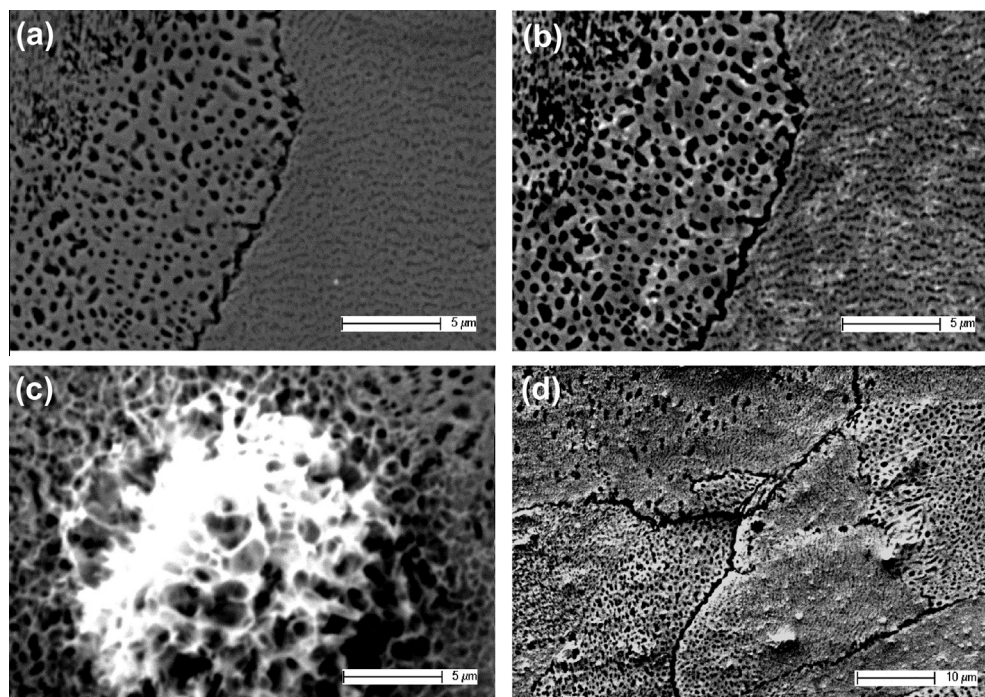
Fig. 3. (a) SEM images of unexposed Galfan surface; (b) the same area exposed after 1 wet/dry cycle at 90% RH without NaCl; (c) morphology of a carbonate-rich corrosion product after 1 wet/dry cycle; and (d) a given surface after 2 wet/dry cycles at 90% RH without NaCl.
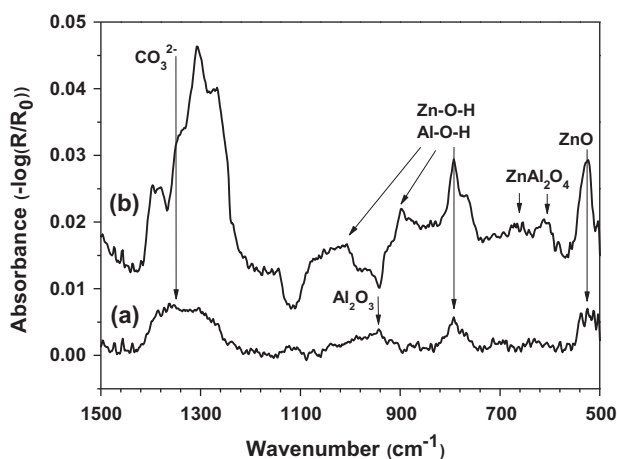
Fig. 4. In situ IRAS spectrum obtained after exposure for 1 (a) and 2 (b) wet/dry cycles at 90% RH without NaCl pre-deposition.

the IRAS data after two wet/dry cycles with SEM/EDS investigations (Fig. 3d), the amount of corrosion products, presumably ZnO and $Zn_6Al_2(OH)_{16}CO_3 \cdot 4H_2O$ after one wet/dry cycle, was considerably increased. The detection of Al, Zn, O and C in the cluster-like corrosion product seen in Fig. 3c may well support the existence of $Zn_6Al_2(OH)_{16}CO_3 \cdot 4H_2O$, whereby the cluster-like structure may have formed through accelerated formation of the thread-like features in localized areas. However, the assignment of phases by IRAS cannot be performed unambiguously and there is also the possibility of amorphous $Zn_5(CO_3)_2(OH)_6$ formation, a corrosion product known to form in very early stages of the atmospheric corrosion of zinc.

In order to find further evidence for phases formed during initial exposure conditions, the same wet/dry exposures were also performed at 70% RH and analysed by means of both SEM and in situ IRAS after wet/dry cycles. Only very few morphological changes due to corrosion product formation could be observed.

The predominant peaks observed by IRAS were assigned to ZnO ($530 \, cm^{-1}$), $ZnAl_2O_4$ ($660 \, cm^{-1}$) and Al_2O_3 ($960 \, cm^{-1}$ [30]). A peak located at $1106 \, cm^{-1}$ may be assigned to OH stretching vibration in hydroxides such as $Zn(OH)_2$ and/or $Al(OH)_3$ [21,49,50]. In general oxides and hydroxides were the dominant phases at 70% RH, while the peaks assigned to $Zn_6Al_2(OH)_{16}CO_3 \cdot 4H_2O$ could only be observed after 8 cycles of exposure. Any confirmation of the preferential formation of Al_2O_3 in the more aluminum-rich β-Al phase cannot be made by means of IRAS because of its lack in lateral resolution.

In all, the formation of corrosion products at the humid/dry conditions resulted in the formation of a very thin layer of corrosion products, possibly consisting of ZnO, Al_2O_3 and $ZnAl_2O_4$ and also in more visible thread-like corrosion products tentatively assigned to $Zn_6Al_2(OH)_{16}CO_3 \cdot 4H_2O$. The latter phase was locally forming larger clusters of corrosion products. Corrosion products were preferentially formed (as indicated by SEM) in the η-Zn phase adjacent to the β-Al phase.

3.2. Effect of humidity and predeposited NaCl on initial corrosion of Galfan

The following section explores the influence of both humidity and sodium chloride (NaCl) deposition on the initial atmospheric corrosion of Galfan. We first show images obtained by ESEM, displaying the gradual deliquescence of individual predeposited NaCl crystals at in situ conditions, followed by the same detailed morphological and chemical characterization of corrosion products by SEM and IRAS as in the previous section.

Fig. 5a, obtained under high vacuum conditions, displays micrometer-sized NaCl crystals distributed along the Galfan surface with predeposited NaCl ($4 \, \mu g/cm^2$). Fig. 5b is obtained at 40% RH and shows how the NaCl crystals seem to slightly change in shape and in some cases also increase in size. At 70% RH, Fig. 5c, the crystals have completely turned into droplets. This RH is close to the point of deliquescence of NaCl, but evidence
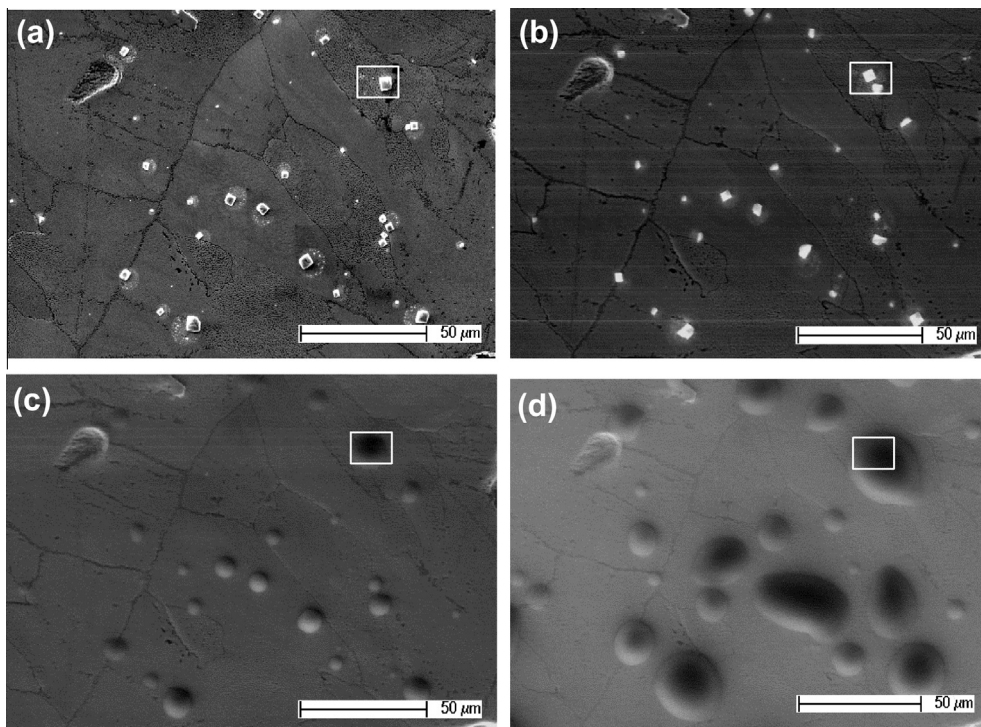
Fig. 5. ESEM images of Galfan surface with 4 µg/cm^2 predeposited NaCl particles and increasing relative humidity (RH). (a) 0% RH; (b) 40% RH; (c) 70% RH and (d) 90% RH.

has been reported that water and NaCl can interact at lower RH than the deliquescence point [51]. At 90% RH, Fig. 5d, the NaCl droplets further spread, most likely due to secondary spreading effects [52], and gradually covered most of the surface.

Similar to the previous section, parallel wet/dry exposures with NaCl pre-deposition of Galfan were performed and the corrosion products analysed by means of SEM and in situ IRAS. Fig. 6a reveals the same Galfan surface as shown in Fig. 5a–d after one wet/dry cycle exposure at 90% RH. Compared to the same conditions without NaCl (Fig. 3b), the presence of NaCl clearly resulted in accelerated corrosion and the entire Galfan surface became more or less covered with corrosions products. Fig. 6b displays a selected area of Fig. 6a at higher magnification and shows a high frequency of smaller rounded corrosion products, primarily formed in the η-Zn phase between areas of the β-Al phase. After two wet/dry cycles of exposure, Fig. 7c, the surface was completely covered by corrosion products of relatively uniform thickness, whereas some areas formed clusters of much thicker corrosion products, Fig. 7d. EDS-analysis revealed Zn, Al, O and Cl to be the main elements of these clusters.

Fig. 7 displays the corresponding in situ IRAS spectra after one (lower curve) and two (upper curve) wet/dry cycles. Several peaks that appeared without NaCl (Fig. 4) were also observed upon NaCl exposure, including the peaks for $ZnAl_2O_4$ (560–670 cm^{-1}), the peak at 1143 cm^{-1} tentatively assigned to $Zn(OH)_2$ or $Al(OH)_3$ [21,49,50], and the major peak at 1370 cm^{-1} assigned to CO_3^{2-} in $Zn_6Al_2(OH)_{16}CO_3 \cdot 4H_2O$ [26], similar to findings at the humid conditions without NaCl. Three major peaks in the range from 700 to 1100 cm^{-1} were observed for samples exposed both with and without NaCl. While two of the peaks were positioned at the same wavenumbers (900 and 1015 cm^{-1}) the third peak at 730 cm^{-1} was significantly shifted (62 cm^{-1}) compared with observations without NaCl. The presence of these three peaks, identified as Zn–O–H and Al–O–H vibrations, may form evidence of the formation of another layered double hydroxide such as $Zn_2Al(OH)_6$

$Cl \cdot 2H_2O$ [53] and/or $Zn_5(OH)_8Cl_2 \cdot H_2O$ [21]. It was however not possible to distinguish these phases from each other.

In all, predeposited NaCl resulted in increased corrosion of Galfan under current exposure conditions. Similar to the exposure without NaCl, corrosion products were initially observed in the slightly Zn-richer η-Zn phase, but spread along the surface to cover most of the Galfan surface after two wet/dry cycles. Although phase identification with IRAS cannot be performed unambiguously, it suggests that both carbonate- and chloride-containing phases have been formed.

3.3. Short and long-term corrosion effects of Galfan in marine field exposures

Having analyzed the corrosion products obtained under present laboratory exposure conditions with humidified air and predeposited chlorides as corrosion stimulators, we compare next the results of corrosion products formation with those obtained for Galfan under outdoor marine exposure conditions. Non-treated surfaces of as received Galfan coatings were exposed at unsheltered conditions at the marine site of Brest, France, and the corrosion product formation was analyzed by the complementary techniques SEM/EDS, CRM, IRAS and GIXRD.

SEM revealed similar corrosion product morphologies of Galfan surfaces after short term (2 and 4 weeks) marine exposures, Fig. 8a–d, as after current laboratory exposures, Fig. 6. The initial corrosion frequently started in the η-Zn phase and grew into clusters of corrosion products. EDS-analysis revealed that the cluster-like corrosion products in Fig. 8c mainly contained Zn, Al, O and C, and possibly consisted of ZnO or $Zn_6Al_2(OH)_{16}CO_3 \cdot 4H_2O$ because of their compositional and morphological resemblance with the corrosion products seen in Fig. 3c. A different sheet-like corrosion product displayed in Fig. 8b after 2 weeks and (d) after 4 weeks contained significant amounts of Cl, besides Al, Zn and O, and may consist of chloride-rich corrosion products, such as Na_4Zn_4
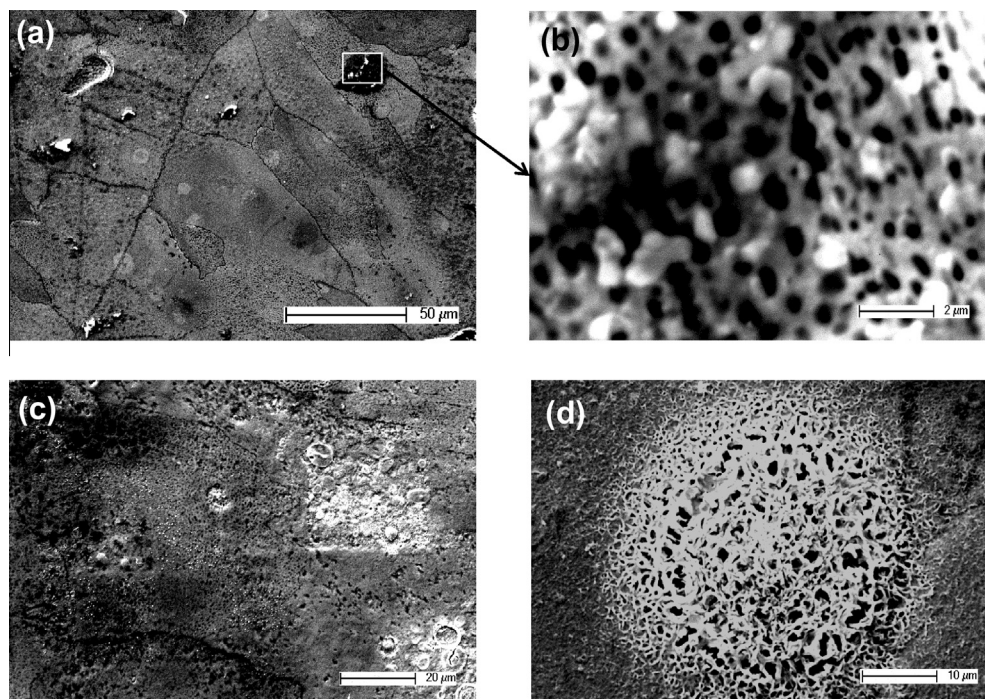
Fig. 6. SEM images of Galfan surface with 4 µg/cm^2 predeposited NaCl particles. (a) is the same surface as in Fig. 5a after 1 wet/dry cycle exposure at 90% RH with NaCl; (b) is a magnified corroded section of (a); (c) is a given surface after 2 wet/dry cycles at 90% RH with NaCl; and (d) is a chloride-rich corrosion product cluster after 2 wet/dry cycles.
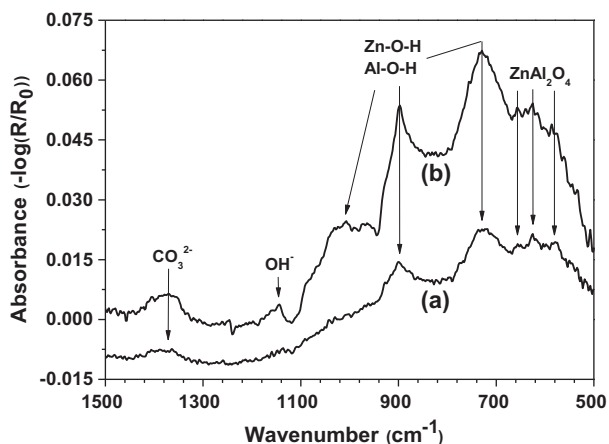
Fig. 7. In situ IRAS spectrum obtained after exposure for 1(a) and 2 (b) wet/dry cycles at 90% RH with NaCl pre-deposition.

$SO_4(OH)_6Cl_2 \cdot 6H_2O$, $Zn_2Al(OH)_6Cl \cdot 2H_2O$ and/or $Zn_5(OH)_8Cl_2 \cdot H_2O$ [54].

Table 1 displays all corrosion products identified after non-sheltered marine exposure of Galfan during 2, 4, 12, 26 weeks, 1 and 5 years, and corresponding analytical support for each phase as based on IRAS, CRM or GIXRD. After 2 weeks there is strong evidence for ZnO, $ZnAl_2O_4$ and Al_2O_3. After 4 weeks there is evidence also for amorphous $Zn_6Al_2(OH)_{16}CO_3 \cdot 4H_2O$ and indications of crystalline chloride-containing phases, namely $Na_4Zn_4SO_4(OH)_6Cl_2 \cdot 6H_2O$ and $Zn_5Cl_2(OH)_6 \cdot H_2O$ and/or $Zn_2Al(OH)_6Cl \cdot H_2O$, two phases hard to distinguish from each other. However after five years, the only crystalline phase detected is $Zn_6Al_2(OH)_{16}CO_3 \cdot 4H_2O$, which was observed in an amorphous state upon shorter exposures.

Table 1 also lists all phases detected after current laboratory exposures. With the exception of $Na_4Zn_4SO_4(OH)_6Cl_2 \cdot 6H_2O$, the relatively simple laboratory exposure of Galfan consisting of predeposited NaCl and two wet/dry cycles seems to generate the most important phases identified after the long term marine field exposure of Galfan, although in different amounts and proportions.

4. Discussion

4.1. Microstructure of Galfan and corrosion initiation

We consider first the results without any pre-deposition of NaCl. Exposure to two wet/dry cycles at 70% RH resulted in the formation of very thin oxides identified mainly as ZnO, Al_2O_3 and $ZnAl_2O_4$, most likely covering the entire Galfan surface. At 90% RH, ZnO and $Zn_6Al_2(OH)_{16}CO_3 \cdot 4H_2O$ were the dominating phases. Visible corrosion products observed by means of SEM seem to start forming in the slightly Zn-richer η-Zn phase adjacent to the β-Al phase. Due to its slightly higher Al-content the β-Al phase could be expected to be the anode, but oxide formation seems to reverse the conditions so that the β-Al phase acts more noble than η-Zn phase.

With prolonged exposure, the corrosion products develop with a thread-like appearance, starting in the η-Zn phase followed by its subsequent growth over the entire Galfan surface and with $Zn_6Al_2(OH)_{16}CO_3 \cdot 4H_2O$ as the dominating phase. OH$^-$-production in cathodic areas results in a local pH-increase in the aqueous adlayer, instability of Al_2O_3, enhanced Al-dissolution and the formation of local clusters of $Zn_6Al_2(OH)_{16}CO_3 \cdot 4H_2O$, as revealed in Fig. 3c. The fact that a phase with such complicated structure can form already in the initial stages of corrosion product evolution suggest that it forms directly in the aqueous adlayer through a reaction with all ions involved, rather than through a gradual process with several dissolution–precipitation steps, as is often the case in, e.g., outdoor atmospheric corrosion [58]. $Zn_6Al_2(OH)_{16}CO_3 \cdot 4H_2O$ has previously been identified as a corrosion product on Galfan and other Zn-based coatings [59–61]. It consists of layered double hydroxide [62] sheets of octahedrons, each composed of Zn(II) or
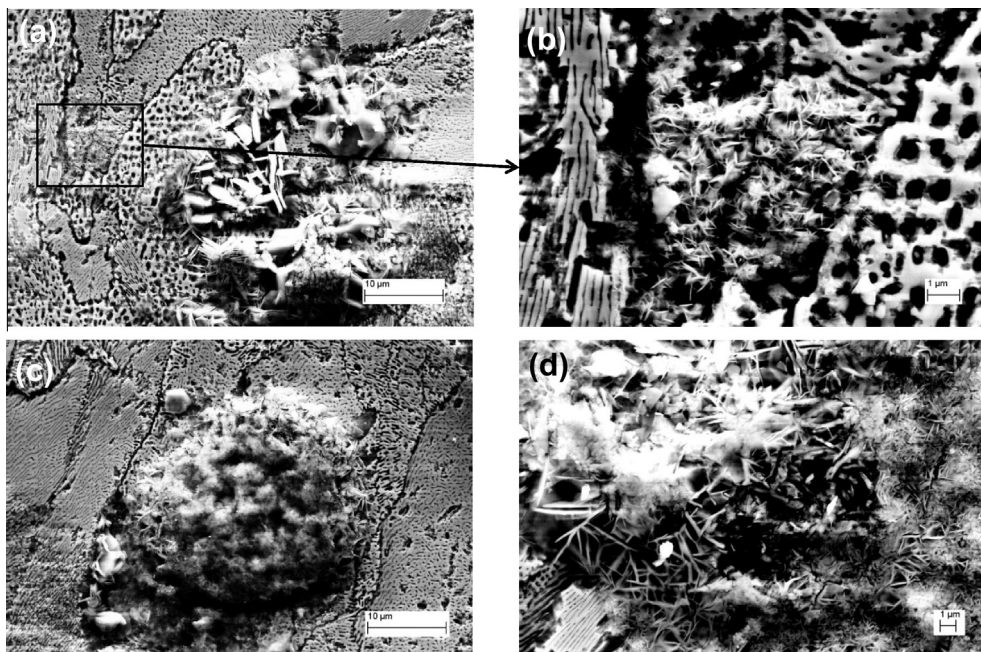
Fig. 8. (a) SEM image of corrosion products on Galfan exposed for 2 weeks in the marine site; (b) is a selected area of (a) at higher magnification; (c) shows a carbonate-rich corrosion product after 2 weeks and (d) chloride-rich corrosion products after 4 weeks.

Table 1
Compilation of corrosion product evolution identified by means of IRAS, CRM and GIXRD of Galfan exposed during 5 years at a marine test site and in parallel laboratory exposures.

Exposure period	IRAS	CRM	GIXRD	Identified phases
2 weeks	ZnO (530 cm^{-1}, [21]), ZnAl$_2$O$_4$[a] (660 cm^{-1}, [46,47]), OH$^-$/SO$_4^{2-}$ (1100 cm^{-1}, [21,49,50])	ZnO (325–475 cm^{-1}, 475–625 cm^{-1}, [45]), Al$_2$O$_3$/ZnAl$_2$O$_4$ (325–475 cm^{-1}, 600–800 cm^{-1}, [55–57])	None	ZnO, Al$_2$O$_3$/ZnAl$_2$O$_4$, Zn(OH)$_2$/Al(OH)$_3$[a], Na$_4$Zn$_4$SO$_4$(OH)$_6$Cl$_2$·6H$_2$O, Zn$_5$Cl$_2$(OH)$_6$·H$_2$O/ Zn$_2$Al(OH)$_6$Cl·H$_2$O, Zn$_6$Al$_2$(OH)$_{16}$CO$_3$·4H$_2$O
4 weeks	ZnO, ZnAl$_2$O$_4$[a], OH$^-$/SO$_4^{2-}$, CO$_3^{2-}$ (1350 cm^{-1}, [26,44])	ZnO, Al$_2$O$_3$/ZnAl$_2$O$_4$	Na$_4$Zn$_4$SO$_4$(OH)$_6$Cl$_2$·6H$_2$O[a], Zn$_5$Cl$_2$(OH)$_6$·H$_2$O/ Zn$_2$Al(OH)$_6$Cl·H$_2$O[a]	
12 weeks	ZnO, ZnAl$_2$O$_4$[a], OH$^-$/SO$_4^{2-}$, CO$_3^{2-}$	ZnO, Al$_2$O$_3$/ZnAl$_2$O$_4$	Na$_4$Zn$_4$SO$_4$(OH)$_6$Cl$_2$·6H$_2$O[a], Zn$_5$Cl$_2$(OH)$_6$·H$_2$O/ Zn$_2$Al(OH)$_6$Cl·H$_2$O[a]	
26 weeks	ZnO, ZnAl$_2$O$_4$[a], OH$^-$/SO$_4^{2-}$, CO$_3^{2-}$	ZnO, Al$_2$O$_3$/ZnAl$_2$O$_4$, CO$_3^{2-}$ (1000–1100 cm^{-1}, [45])	Na$_4$Zn$_4$SO$_4$(OH)$_6$Cl$_2$·6H$_2$O[a], Zn$_5$Cl$_2$(OH)$_6$·H$_2$O/ Zn$_2$Al(OH)$_6$Cl·H$_2$O[a]	
1 year	ZnO, ZnAl$_2$O$_4$[a], OH$^-$/SO$_4^{2-}$, CO$_3^{2-}$, Zn–O–H/Al–O–H (790 cm^{-1}, [21,26])	ZnO, Al$_2$O$_3$/ZnAl$_2$O$_4$, CO$_3^{2-}$, SO$_4^{2-}$ (900–1000 cm^{-1}, [45])	Zn$_5$Cl$_2$(OH)$_6$·H$_2$O/ Zn$_2$Al(OH)$_6$Cl·H$_2$O[a]	
5 years	ZnO, ZnAl$_2$O$_4$[a], OH$^-$/SO$_4^{2-}$, CO$_3^{2-}$, Zn–O–H/Al–O–H (727, 895, 1001 cm^{-1}, [21,53])	ZnO, Al$_2$O$_3$/ZnAl$_2$O$_4$, CO$_3^{2-}$, SO$_4^{2-}$	Zn$_6$Al$_2$(OH)$_{16}$CO$_3$·4H$_2$O	
Laboratory exposure	Al$_2$O$_3$ (945 cm^{-1}, [30]), ZnO, ZnAl$_2$O$_4$[a], OH$^-$, CO$_3^{2-}$, Zn–O–H/ Al–O–H	–	–	ZnO, Al$_2$O$_3$/ZnAl$_2$O$_4$, Zn(OH)$_2$/Al(OH)$_3$[a], Zn$_5$Cl$_2$(OH)$_6$·H$_2$O/Zn$_2$Al(OH)$_6$Cl·H$_2$O[a], Zn$_6$Al$_2$(OH)$_{16}$CO$_3$·4H$_2$O[a]

[a] Tentative phases.

Al(III)-ions, which are coordinated octahedrally to six OH$^-$-ions. Charged ions such as CO$_3^{2-}$-ions are easily incorporated into the interlayer spacing and hold together the sheets. Layered double hydroxides exhibit a high affinity to CO$_3^{2-}$-ions [44]. It is interesting to note that Zn$_6$Al$_2$(OH)$_{16}$CO$_3$·4H$_2$O was formed under current laboratory exposure conditions, despite the fact that the CO$_2$-content was reduced to much lower concentration (<20 ppm) than in ambient conditions (≈350 ppm).

We consider next exposures of Galfan with predeposited NaCl. Fig. 5 displays the distribution of predeposited NaCl (a) and of droplets (c and d) after the point of deliquescence of NaCl has been reached. The circular shape of most droplets obtained with ESEM under in situ conditions suggests that the wetting process is the same along the whole Galfan surface, irrespective of the microstructure beneath. Also when analyzing the same corroded surface with regular SEM under vacuum conditions, Fig. 6a, the rounded

features that correspond to the droplets in Fig. 5d seem to cover parts of the Galfan surface independent of the grains and other microstructural features. However, when studying a corroded area at higher magnification, Fig. 6b, visible rounded corrosion products of larger size and frequency were observed compared to exposures without predeposited NaCl, Fig. 3b. Similar to the case without NaCl, these early corrosion products were observed primarily at the η-Zn phase between areas of the β-Al phase and suggest that the η-Zn phase acts as anode. Local clusters of thicker corrosion products, Fig. 6d, either composed of $Zn_2Al(OH)_6Cl \cdot 2H_2O$ and/or $Zn_5(OH)_8Cl_2 \cdot H_2O$, as revealed from IRAS. In addition, the IRAS-spectra also revealed the formation of $Zn_6Al_2(OH)_{16}CO_3 \cdot 4H_2O$. With pre-deposition of NaCl particles, the corrosion behavior of Galfan coating was largely accelerated and formation of chloride-rich corrosion products was dominant.

Following a general description [63], chloride ions compete with surface hydroxyl groups in the oxides present, which results in local depassivation and areas that are more susceptible to transient active dissolution of metal ions [63,64]. Similar to the case without NaCl, the ample dissolution of both Zn^{2+} and Al^{3+} creates conditions for fast formation of $Zn_6Al_2(OH)_{16}CO_3 \cdot 4H_2O$, a phase previously reported on Galfan in chloride-containing environments [59–61]. Due to its specific crystal structure, $Zn_6Al_2(OH)_{16}CO_3 \cdot 4H_2O$ possesses ion-exchange properties [65] where chloride ions can replace carbonate ions in the interlayer spacing and become inactive for further repassivation of the Galfan surface [29]. In agreement with this, the $Zn_6Al_2(OH)_{16}CO_3 \cdot 4H_2O$ phase was recently suggested to be the main reason for the enhanced corrosion resistance of Zn–Al–Mg coatings over more conventional hot-dip galvanized zinc coatings [59].

4.2. General scenario for corrosion product evolution on Galfan

Earlier studies on the atmospheric corrosion of bare Zn metal have revealed commonly occurring sequences of how the most frequent phases are formed in different types of environments [17]. It is of interest to compare the earlier proposed sequence of corrosion products formed on bare Zn and Al metal in chloride containing atmospheres (sheltered conditions) with findings for the investigated Zn-alloy coatings of Galfan (present work). The results are compiled in Fig. 9 in which a generalized evolution scheme of corrosion products is proposed for bare Zn sheet [17], Al sheet [22,66] and for Zn–Al coatings exposed to atmospheric marine environments (unsheltered conditions). Zinc and aluminum oxides and/or hydroxides form instantaneously in moist atmosphere on all materials. In contact with the CO_2-containing atmosphere the hydroxides react and form Hydrozincite ($Zn_5(CO_3)_2(OH)_6$) and Hydrotalcite ($Zn_6Al_2(OH)_{16}CO_3 \cdot 4H_2O$). High chloride deposition
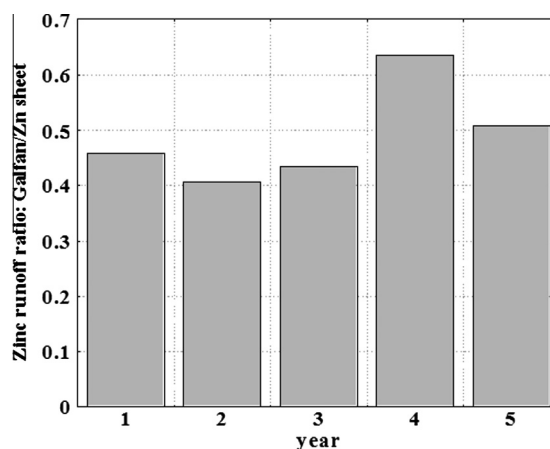

Fig. 10. Ratio of annual runoff rates of zinc from Galfan compared with zinc runoff from bare zinc sheet during five years of unsheltered marine exposure (45° facing south) in Brest, France.

rates result in the subsequent formation of hydroxychlorides, Simonkolleite ($Zn_5(OH)_8Cl_2 \cdot H_2O$) on bare Zn metal and $Zn_2Al(OH)_6Cl \cdot 2H_2O$ and/or $Zn_5(OH)_8Cl_2 \cdot H_2O$ on the Zn–Al coatings. As all hydroxycarbonates and hydroxychlorides bear structural resemblance and consist of layered structures with the layers held together by anions, such as carbonate, chloride and/or sulfate, the evolution from one phase to another can proceed through ion-exchange mechanisms, as previously proposed by Odnevall and Leygraf [17]. Marine environments are not only characterized by ample chloride deposition, but also by sulfate deposition, e.g. from sea spray and gaseous SO_2 [54]. As a result, another phase characterized by a layered structure has been found after longer exposure times on both pure Zn and Galfan, $Na_4Zn_4SO_4(OH)_6Cl_2 \cdot 6H_2O$.

The proposed reaction scheme can be of significance for explaining various characteristic corrosion-related properties for the materials. One example is the long-term zinc release pattern induced by the interaction of humidity and rainwater on the surface. Fig. 10 shows the ratio between the annual released amounts of zinc from bare zinc sheet compared with the release of zinc from Galfan, exposed in parallel during the 5-year exposure period. The results clearly show a significantly lower (approximately twice as low) released amount of zinc from Galfan compared to bare zinc sheet throughout the exposure period, despite the fact that zinc-rich phases dominate the patina on both zinc and Galfan also after longer exposure time periods. Detailed corrosion product analysis reveal ZnO and $Zn_5(CO_3)_2(OH)_6$ to be the main patina constituents on bare zinc sheet [45] and $Zn_6Al_2(OH)_{16}CO_3 \cdot 4H_2O$ the main

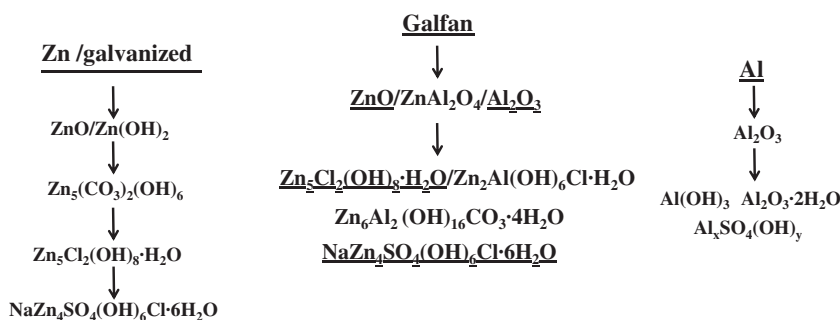Fig. 9. Sequence of phases observed in corrosion products formed on Zn sheet (left, [17]), Galfan (middle, this study) and Al (right, [22], [66]) upon long-term exposure in marine environments. Vertical arrows indicate the evolution of one phase into the next phase. Phases without vertical arrow can exist simultaneously next to each other. Underlined phases are also observed in corresponding sequences for bare Zn and bare Al metals.

constituent on Galfan (this study). Reduced (approximately by a factor of two) release rates of zinc from Galfan (forming $Zn_6Al_2(OH)_{16}CO_3\cdot 4H_2O$) compared with bare zinc sheet (forming $Zn_5(CO_3)_2(OH)_6$) was also evident during a 10 year urban field exposure at unsheltered conditions [67]. Improved barrier properties of corrosion products formed on Galfan compared to galvanized steel in chloride-rich environments have also been elucidated in the literature [59].

The reaction scheme was shown to be valid for corrosion product formation in the N-VDA-test (New revised VDA Corrosion Test Method, Standard SEP 1850 VDA 621-415 B), where the target was to evaluate an accelerated corrosion test of Zn–Al coatings on steel for automotive applications [35]. $Zn_6Al_2(OH)_{16}CO_3\cdot 4H_2O$ and $Zn_2Al(OH)_6Cl\cdot 2H_2O$ and/or $Zn_5(OH)_8Cl_2\cdot H_2O$ were formed in the initial stages of the accelerated test and dominated the patina on Galfan, whereas $Zn_5(CO_3)_2(OH)_6$ and $Zn_5(OH)_8Cl_2\cdot H_2O$ were the main patina constituents of bare zinc sheet. After longer exposure periods, $Zn_5(CO_3)_2(OH)_6$ was also formed on Galfan.

5. Conclusions

1. A clear influence of microstructure on corrosion initiation of Galfan has been observed upon laboratory exposure to cyclic humidified air with or without predeposited NaCl. Corrosion product formation starts in the η-Zn phase adjacent to the β-Al phase. The corrosion products then spread to adjacent zinc-richer regions following the direction of lamellas or rods, and locally forming clusters of corrosion products with characteristic features.

2. The phases identified in the laboratory exposures with cyclic humidity conditions and predeposited NaCl include the initial formation of ZnO, $ZnAl_2O_4$ and Al_2O_3 and subsequent formation $Zn_6Al_2(OH)_{16}CO_3\cdot 4H_2O$, and $Zn_2Al(OH)_6Cl\cdot 2H_2O$ and/or $Zn_5Cl_2(OH)_8\cdot H_2O$. Atmospheric corrosion of Galfan coating was largely accelerated with pre-deposition of NaCl particles.

3. The same phases are also identified on Galfan upon five years of non-sheltered marine exposure in Brest, France. The exception is $Na_4Zn_4SO_4(OH)_6Cl_2\cdot 6H_2O$, which is formed at field conditions but not during laboratory exposures. Hence, the investigated laboratory exposure is able to reproduce most phases found in the marine exposure, however in different proportion and coverage of the phases identified.

4. Based on the combined laboratory and field exposures a general scenario for corrosion product evolution on Galfan in chloride-containing atmospheric environments is proposed, which can aid in the understanding of important characteristic corrosion-related properties of Galfan.

5. An important phase found on Galfan under current exposure conditions is the layered double hydroxide $Zn_6Al_2(OH)_{16}CO_3\cdot 4H_2O$, which largely governs the long-term runoff rates of zinc from Galfan (reduced by a factor of two compared to bare zinc sheet) in the marine exposure.

References

[1] X.G. Zhang, Corrosion and Electrochemistry of Zinc, Plenum Press, New York, 1996.
[2] ArcelorMittal, Steels coated with Galfan zinc–aluminum alloy, 2008.
[3] S.T. Bluni, A.R. Marder, J.I. Goldstein, Surface characterization of hot-dip Galfan coatings, Mater. Charact. 33 (1994) 93–97.
[4] J. Murray, The Al–Zn (aluminum–zinc) system, J. Phase Equilib. 4 (1983) 55–73.
[5] A.R. Marder, The metallurgy of zinc-coated steel, Prog. Mater. Sci. 45 (2000) 191–271.
[6] J. Elvins, J.A. Spittle, D.A. Worsley, Relationship between microstructure and corrosion resistance in Zn–Al alloy coated Galvanised steels, Corros. Eng. Sci. Technol. 38 (2003) 197–204.
[7] M. Żelechower, J. Kliś, E. Augustyn, J. Grzonka, D. Stróż, T. Rzychoń, H. Woźnica, The microstructure of annealed Galfan coating on steel substrate, Arch. Metall. Mater. 57 (2012) 517–523.
[8] G.A. López, E.J. Mittemeijer, B.B. Straumal, Grain boundary wetting by a solid phase; microstructural development in a Zn–5 wt.% Al alloy, Acta Mater. 52 (2004) 4537–4545.
[9] J. Elvins, J.A. Spittle, D.A. Worsley, Microstructural changes in zinc aluminum alloy Galvanising as a function of processing parameters and their influence on corrosion, Corros. Sci. 47 (2005) 2740–2759.
[10] A.E. Ares, L.M. Gassa, Corrosion susceptibility of Zn–Al alloys with different grains and dendritic microstructures in Nacl solutions, Corros. Sci. 59 (2012) 290–306.
[11] W.R. Osório, C.M. Freire, A. Garcia, The effect of the dendritic microstructure on the corrosion resistance of Zn–Al alloys, J. Alloys Compd. 397 (2005) 179–191.
[12] E. Almeida, M. Morcillo, B. Rosales, Atmospheric corrosion of zinc Part 1: rural and urban atmospheres, Brit. Corros. J. 35 (2000) 284–288.
[13] E. Almeida, M. Morcillo, B. Rosales, Atmospheric corrosion of zinc Part 2: marine atmospheres, Brit. Corros. J. 35 (2000) 289–296.
[14] D. de la Fuente, J.G. Castaño, M. Morcillo, Long-term atmospheric corrosion of zinc, Corros. Sci. 49 (2007) 1420–1436.
[15] T.E. Graedel, Corrosion mechanisms for zinc exposed to the atmosphere, J. Electrochem. Soc. 136 (1989) 193C–203C.
[16] T.H. Muster, A. Bradbury, A. Trinchi, I.S. Cole, T. Markley, D. Lau, S. Dligatch, A. Bendavid, P. Martin, The atmospheric corrosion of zinc: the effects of salt concentration, droplet size and droplet shape, Electrochim. Acta 56 (2011) 1866–1873.
[17] I. Odnevall, C. Leygraf, Reaction Sequences in Atmospheric Corrosion of Zinc, American Society for Testing and Materials, Philadelphia, PA, ETATS-UNIS, 1995.
[18] F. Zhu, X. Zhang, D. Persson, D. Thierry, In situ infrared reflection absorption spectroscopy studies of confined zinc surfaces exposed under periodic wet–dry conditions, Electrochem. Solid-State Lett. 4 (2001) B19–B22.
[19] T. Aastrup, C. Leygraf, Simultaneous infrared reflection absorption spectroscopy and quartz crystal microbalance measurements for in situ studies of the metal/atmosphere interface, J. Electrochem. Soc. 144 (1997) 2986–2990.
[20] N.S. Azmat, K.D. Ralston, B.C. Muddle, I.S. Cole, Corrosion of Zn under acidified marine droplets, Corros. Sci. 53 (2011) 1604–1615.
[21] Z.Y. Chen, D. Persson, C. Leygraf, Initial NaCl-particle induced atmospheric corrosion of zinc-Effect of CO_2 and SO_2, Corros. Sci. 50 (2008) 111–123.
[22] J.J. Friel, Atmospheric corrosion products on AlZn and AlZn metallic coatings, Corrosion 42 (1986) 422–426.
[23] S.A. Matthes, S.D. Cramer, S.J. Bullard, B.S. Covino, B.S. Covino Jr, G.R. Holcomb, Atmospheric corrosion and precipitation runoff from zinc and zinc alloy surfaces, in: NACE Corrosion Conference, San Diego, CA (US), 2003.
[24] I. Odnevall Wallinder, C. Leygraf, C. Karlén, D. Heijerick, C.R. Janssen, Atmospheric corrosion of zinc-based materials: runoff rates, chemical speciation and ecotoxicity effects, Corros. Sci. 43 (2001) 809–816.
[25] J.C. Zoccola, H.E. Townsend, A.R. Borzillo, J.B. Horton, Atmospheric corrosion resistance of aluminum–zinc alloy-coated steel, in: S.K. Coburn (Ed.), Atmospheric Factors Affecting the Corrosion of Engineering Materials, ASTM STP 646, American Society for Testing and Materials, Philadelphia, Pennsylvania, 1978.
[26] D. Persson, D. Thierry, N. LeBozec, Corrosion product formation on Zn55Al coated steel upon exposure in a marine atmosphere, Corros. Sci. 53 (2011) 720–726.
[27] Y. Li, Formation of nano-crystalline corrosion products on Zn–Al alloy coating exposed to seawater, Corros. Sci. 43 (2001) 1793–1800.
[28] I. Odnevall Wallinder, W. He, P.E. Augustsson, C. Leygraf, Characterization of black rust staining of unpassivated 55% Al–Zn alloy coatings. Effect of temperature, pH and wet storage, Corros. Sci. 41 (1999) 2229–2249.
[29] P. Volovitch, T.N. Vu, C. Allély, A. Abdel Aal, K. Ogle, Understanding corrosion via corrosion product characterization: II. role of alloying elements in

improving the corrosion resistance of Zn–Al–Mg coatings on steel, Corros. Sci. 53 (2011) 2437–2445.

[30] P. Qiu, C. Leygraf, I. Odnevall Wallinder, Evolution of corrosion products and metal release from Galvalume coatings on steel during short and long-term atmospheric exposures, Mater. Chem. Phys. 133 (2012) 419–428.

[31] X. Zhang, T.-N. Vu, P. Volovitch, C. Leygraf, K. Ogle, I. Odnevall Wallinder, The initial release of zinc and aluminum from non-treated Galvalume and the formation of corrosion products in chloride containing media, Appl. Surf. Sci. 258 (2012) 4351–4359.

[32] A.R. Moreira, Z. Panossian, P.L. Camargo, M.F. Moreira, I.C. da Silva, J.E.R. de Carvalho, Zn/55Al coating microstructure and corrosion mechanism, Corros. Sci. 48 (2006) 564–576.

[33] N.-Y. Tang, Y. Liu, Corrosion performance of aluminum-containing zinc coatings, ISIJ Int. 50 (2010) 455–462.

[34] L. Yang, Y. Zhang, X. Zeng, Z. Song, Corrosion behavior of superplastic Zn–Al alloys in simulated acid rain, Corros. Sci. 59 (2012) 229–237.

[35] K.-H. Stellnberger, S. Geisler, Neuer Laborkorrosionstest – relevante Ergebnisse, Journal für Oberflächentechnik 49 (2009) 32ff.

[36] Z.Y. Chen, S. Zakipour, D. Persson, C. Leygraf, Effect of sodium chloride particles on the atmospheric corrosion of pure copper, NACE International, Houston, TX, ETATS-UNIS, 2004. pp. 479–491.

[37] H. Gil, C. Leygraf, Quantitative in situ analysis of initial atmospheric corrosion of copper induced by acetic acid, J. Electrochem. Soc. 154 (2007) C272–C278.

[38] ISO, ISO 17752:2012, Corrosion of metals and alloys – procedures to determine and estimate runoff rates of metals from materials as a result of atmospheric corrosion, 2012.

[39] J. Sandberg, I. Odnevall Wallinder, C. Leygraf, N. Le Bozec, Corrosion-induced zinc runoff from construction materials in a marine environment, J. Electrochem. Soc. 154 (2007) C120–C131.

[40] D. Lindström, I. Odnevall Wallinder, Long-term use of Galvanized steel in external applications. Aspects of patina formation, zinc runoff, barrier properties of surface treatments, and coatings and environmental fate, Environ. Monit. Assess. 173 (2011) 139–153.

[41] T.N. Vu, M. Mokaddem, P. Volovitch, K. Ogle, The anodic dissolution of zinc and zinc alloys in alkaline solution. II. Al and Zn partial dissolution from 5% Al–Zn coatings, Electrochim. Acta 74 (2012) 130–138.

[42] T.E. Madey, J.T.J. Yates., Vibrational Spectroscopy of Molecules on Surfaces, first edition, Methods of Surface Characterization, Springer, 1987.

[43] M.C. Hales, R.L. Frost, Synthesis and vibrational spectroscopic characterisation of synthetic hydrozincite and smithsonite, Polyhedron 26 (2007).

[44] R.L. Frost, A. Soisnard, N. Voyer, S.J. Palmer, W.N. Martens, Thermo-Raman spectroscopy of selected layered double hydroxides of formula $Cu_6Al_2(OH)_{16}CO_3$ and $Zn_6Al_2(OH)_{16}CO_3$, J. Raman Spectrosc. 40 (2009) 645–649.

[45] J. Hedberg, N. Le Bozec, I. Odnevall Wallinder, Spatial distribution and formation of corrosion products in relation to zinc release for zinc sheet and coated pre-weathered zinc at an urban and a marine atmospheric condition, Mater. Corros. (2011) 1–9.

[46] A.A. da Silva, A.d.S. Goncalves, M.R Davolos, Characterization of nanosized $ZnAl_2O_4$ spinel synthesized by the sol–gel method, J. Sol–Gel Sci. Technol. 49 (2009) 101–105.

[47] S. Sunder, S. Rohilla, S. Kumar, P. Aghamkar, Structural characterization of spinel zinc aluminate nanoparticles prepared by coprecipitation method, in: S.K. Tripathi, K. Dharamvir, R. Kumar, G.S.S. Saini, (Eds.), International Conference on Advances in Condensed and Nanomaterials, 2011.

[48] W.-B. Chen, P. Chen, H.Y. Chen, J. Wu, W.-T. Tsai, Development of Al-containing zinc-rich paints for corrosion resistance, Appl. Surf. Sci. 187 (2002) 154–164.

[49] D. Wu, Y. Jiang, J. Liu, Y. Yuan, J. Wu, K. Jiang, D. Xue, Template route to chemically engineering cavities at nanoscale: a case study of $Zn(OH)_2$ template, Nanoscale Res. Lett. 5 (2010) 1779–1787.

[50] H.W. Lee, B.K. Park, M.Y. Tian, J.M. Lee, Relationship between properties of pseudo-boehmite and its synthetic conditions, J. Ind. Eng. Chem. 12 (2006) 295–300.

[51] D. Liang, H.C. Allen, G.S. Frankel, Z.Y. Chen, R.G. Kelly, Y. Wu, B.E. Wyslouzil, Effects of sodium chloride particles, ozone, UV, and relative humidity on atmospheric corrosion of silver, J. Electrochem. Soc. 157 (2010) C146–C156.

[52] Z.Y. Chen, D. Persson, F. Samie, S. Zakipour, C. Leygraf, Effect of carbon dioxide on sodium chloride-induced atmospheric corrosion of copper, J. Electrochem. Soc. 152 (2005) B502–B511.

[53] N. Thomas, M. Rajamathi, Intracrystalline oxidation of thiosulfate-intercalated layered double hydroxides, Langmuir 25 (2009) 2212–2216.

[54] I. Odnevall, C. Leygraf, Formation of $NaZn_4Cl(OH)_6SO_4 \cdot 6H_2O$ in a marine atmosphere, Corros. Sci. 34 (1993) 1213–1229.

[55] S.T. Aruna, V.K.W. Grips, K.S. Rajam, Synthesis and characterization of Ni–Al_2O_3 composite coatings containing different forms of alumina, J. Appl. Electrochem. 40 (2010) 2161–2169.

[56] S. Cava, S.M. Tebcherani, I.A. Souza, S.A. Pianaro, C.A. Paskocimas, E. Longo, J.A. Varela, Structural characterization of phase transition of Al_2O_3 nanopowders obtained by polymeric precursor method, Mater. Chem. Phys. 103 (2007) 394–399.

[57] J. Grabowska, K.K. Nanda, R.T. Rajendra Kumar, J.P. Mosnier, M.O. Henry, S.B. Newcomb, P. McNally, L. O'Reilly, X. Lu, E. McGlynn, Self-organized $ZnAl_2O_4$ nanostructures grown on *c*-sapphire, Superlattices Microstruct. 42 (2007) 327–332.

[58] C. Leygraf, T. Graedel, Atmospheric Corrosion, John Wiley & Sons, New York, 2000.

[59] S. Schürz, G.H. Luckeneder, M. Fleischanderl, P. Mack, H. Gsaller, A.C. Kneissl, G. Mori, Chemistry of corrosion products on Zn–Al–Mg alloy coated steel, Corros. Sci. 52 (2010) 3271–3279.

[60] T. Shimizu, F. Yoshizaki, Y. Miyoshi, A. Andoh, Corrosion products of hot-dip Zn–6%Al–3%Mg coated steel sheet subjected to atmospheric exposure Tetsu to Hagane, J. Iron and Steel Inst. Jpn. 89 (2003) 166–173.

[61] J. Kasperek, D. Verchere, D. Jacquet, N. Phillips, Analysis of the corrosion products on galvanized steels by FTIR spectroscopy, Mater. Chem. Phys. 56 (1998) 205–213.

[62] C.O. Oriakhi, I.V. Farr, M.M. Lerner, Thermal characterization of poly(styrene sulfonate) layered double hydroxide nanocomposites, Clays Clay Miner. 45 (1997) 194–202.

[63] P. Marcus, V. Maurice, H.H. Strehblow, Localized corrosion (pitting): a model of passivity breakdown including the role of the oxide layer nanostructure, Corros. Sci. 50 (2008) 2698–2704.

[64] W. Miao, I.S. Cole, A.K. Neufeld, S. Furman, Pitting corrosion of Zn and Zn–Al coated steels in pH 2 to 12 NaCl solutions, J. Electrochem. Soc. 154 (2007) C7–C15.

[65] F.L. Theiss, M.J. Sear-Hall, S.J. Palmer, R.L. Frost, Zinc aluminum layered double hydroxides for the removal of iodine and iodide from aqueous solutions, Desalin Water Treat. 39 (2012) 166–175.

[66] T.E. Graedel, Corrosion mechanisms for aluminum exposed to the atmosphere, J. Electrochem. Soc. 136 (1989) 204C–212C.

[67] S. Bertling, I. Odnevall Wallinder, C. Leygraf, D. Berggren Kleja, Occurrence and fate of corrosion-induced zinc in runoff water from external structures, Sci. Total Environ. 367 (2006) 908–923.